Quantifying Competitive Degradation Processes in Supported Nanocatalyst Systems

James P. Horwath,[†] Peter W. Voorhees,[‡] and Eric A. Stach[*,†]

[†] *University of Pennsylvania, Department of Materials Science and Engineering, Philadelphia, PA 19104*

[‡] *Northwestern University, Department of Materials Science and Engineering, Evanston, IL 60208*

E-mail: stach@seas.upenn.edu

Abstract

The stability of supported metal nanoparticles determines the activity and lifetime of heterogeneous catalysts. Catalysts can destabilize through several thermodynamic and kinetic pathways, and the competition between these mechanisms complicates efforts to quantify and predict the overall evolution of supported nanoparticles in reactive environments. Pairing *in situ* Transmission Electron Microscopy with unsupervised machine learning, we quantify the destabilization of hundreds of supported Au nanoparticles in real-time to develop a model describing the observed particle evolution as a competition between evaporation and surface diffusion. Data mining of particle evolution statistics allows us to determine physically reasonable values for the model parameters, quantify the particle size at which the Gibbs-Thompson pressure accelerates the evaporation process, and explore how individual particle interactions deviate from the mean-field model. This approach can be applied to a wide range of supported nanoparticle systems, allowing quantitative insight into the mechanisms that control their evolution in reactive environments.

KEYWORDS: *in situ* Transmission Electron Microscopy, catalyst stability, data mining, supported catalysts

Supported metal nanoparticles represent an important class of heterogeneous catalysts. While their high surface to volume ratio and under-coordinated surface sites allow high catalytic activity, these same features lead to instability under common reaction conditions, causing loss of catalytic activity by a variety of mechanisms.[1,2] The decades-long study of evolution processes of small particles has produced theoretical treatments which describe the strong relationship between interfacial energy and particle stability at the nanoscale. However, the difficulty in experimentally observing dynamic systems with sufficiently high spatial and temporal resolution has limited our ability to validate proposed theories and to develop a comprehensive understanding of how equilibrium particle size depends on factors such as temperature, composition, ambient conditions, and local environments.[3–7] Moreover, even with sufficient experimental capabilities, advanced data analysis methods are needed to detect interactions between particles. In fact, nearly 50 years ago, Heinemann and Poppa suggested that clarification of coarsening and mass transport mechanisms in systems of supported nanoparticles would require ”...highly accurate, statistical, nearest neighbor measurements and evaluations of individual particle changes at short time intervals...”[8] Advancements in *in situ* Transmission Electron Microscopy (TEM) enable direct observation of these complicated processes, but the extraction of quantitative information from images remains challenging.[9] Recent research has combined rapid automated image analysis using machine learning with advanced microscopy techniques to study a variety of materials with remarkable detail and precision.[10–13] Here, we quantify the evolution of a model catalyst system at high temperature using *in situ* TEM and automated image analysis. Developing an analytical model for particle growth, we can ascertain the size-dependence of particle growth rates in non-conservative systems and the influence of local and long-range particle interactions.

In this experiment, we use gold nanoparticles supported on amorphous silicon nitride as a model supported catalyst. Particles were specially synthesized to have a narrow particle size distribution, and were capped with dendrimer ligands to aid self-assembly with an ordered structure and specified separation distances.[14,15] Suspended nanoparticles were drop-cast and self-assembled directly on DENSsolutions Wildfire *in situ* heating chips.[16] Subsequently, the sample chip was plasma cleaned at low power under oxygen to remove the ligand coatings, after which the sample was loaded into a FEI Talos S/TEM operating at 200kV and heated to 900°C under vacuum. A survey image of the nanoparticles is shown in Figure 1A.

Previous studies have shown that capping ligands dramatically decrease the temperature required for sintering, so the fact that our nanoparticles retain their shape and position in an ordered array at high temperature indicates that the organic coatings have been completely removed.[17,18] The initial particle size distribution after plasma cleaning is monodisperse, with an average particle size of 4.27 ± 0.34 nm (Supplemental Figure 1). Once at temperature, images were collected every five seconds over the course of an hour. Image segmentation was performed using an unsupervised convolutional neural network to separate background and foreground pixels using a method previously developed by the authors; background information and all code necessary to perform image segmentation is provided in the references.[19–21] Post processing allowed individual particles to be located and labeled, finally resulting in a list of particle sizes and positions as a function of time.[22]

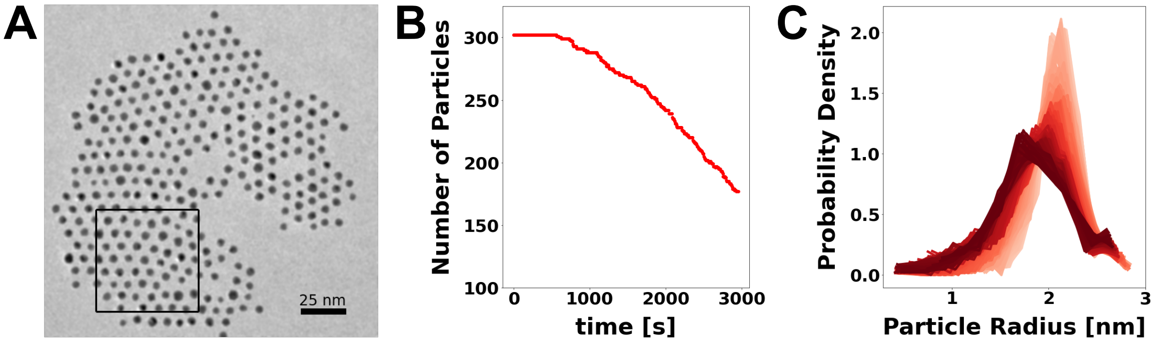

Figure 1: Overview of experimental data showing shrinking particles. A.) shows the as-deposited array of gold nanoparticles. B.) shows the evolution of the particle size distribution as a function of time, where the shade of red darkens as time progresses. C.) shows the number of particles in the image as a function of time.

From Figure 1B and C, it is immediately evident that both the average particle size and the total number of particles decreases with time. Other studies have discussed the evaporation of metallic particles at high temperature, and have described how the evaporation rate depends on the particle size.[23,24] Similarly, recent research has suggested that evaporation and re-deposition of metal atoms is prevalent in oxidation/reduction cycling of supported catalysts.[25] Under our experimental conditions, where continuous pumping of the TEM column creates a non-conservative system, evaporation from the surface of particles is responsible for the observed decrease in particle size and the number of particles on the support. However, we note that evaporation alone cannot be responsible for the observed changes in particle sizes as a function of time. Evidence for this is seen in Figures 2A and 2B. If particles were only subject to evaporation, they would shrink concentrically about their center, with no shifts in particle shape or center of mass (Figure 2A). Our experimental data show changes in center of mass with time, yet these shifts are not significant enough to be consistent with evolution by particle migration and coalescence. Additionally, tracking the growth of individual particles shows crossing growth trajectories even for particles of the same starting size (Figure 2B). These incongruous observations signify the presence of an additional degradation mechanism under our experimental conditions. To account for the anisotropic evolution of particles and potential short range interactions, we developed a model to describe nanoparticle evolution that combines evaporation from the particle surface and mass exchange between particles by diffusion on the support.

The interface velocity of an evaporating particle is given by $v = M\Delta(P - P_e)$.[26] Integrating over the surface of a supported particle yields an expression for the evaporation component of particle growth rate:

$$\frac{dV_{evaporation}}{dt} = M(P - P_e)\beta(\theta)R^2. \tag{1}$$

Here, $M = \alpha\Omega/(2\pi m k_B T)^{1/2}$ is the emission rate of gold from the particle surface (for

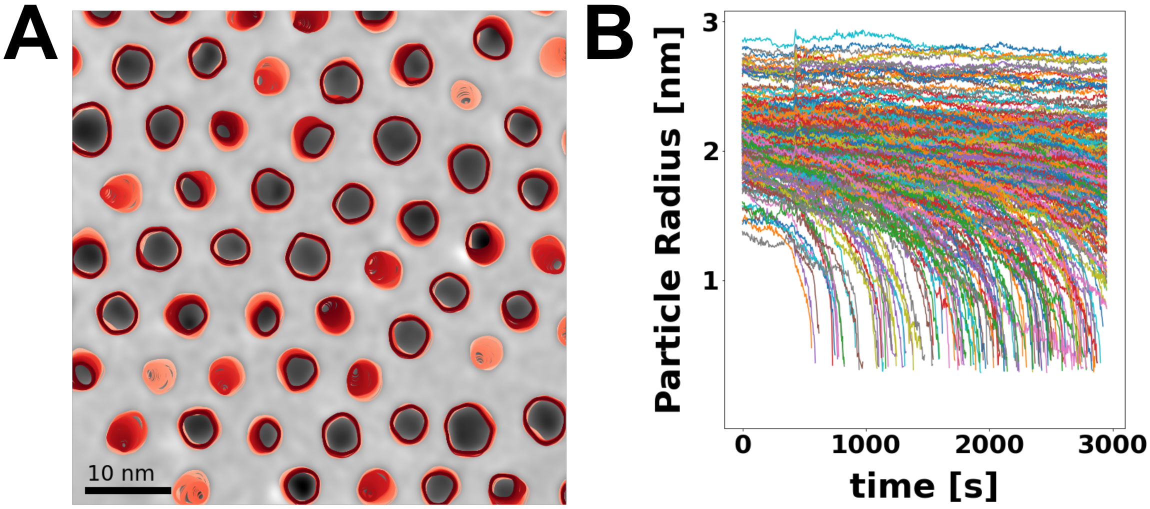

Figure 2: Depiction of changes in particle shape, size, and center of mass through the course of the experiment. In A.) colors colored outlines represent particle boundaries as a function of time, where time increases as color progresses from light to dark red. The particles shown are found in the box outlined in Figure 1A. B.) shows particle size as a function of time for all particles Figure 1A.

dimensionless coefficient α and atomic volume Ω), $P - P_e$ represents the change in Gibbs Free Energy per unit volume for evaporation as a difference between the ambient pressure P and the equilibrium vapor pressure at the particle interface P_e, $\beta(\theta)$ gives the surface area of a truncated sphere as a function of contact angle θ, and R is the particle radius. Further, P_e is modified to account for excess vapor pressure at a curved interface using the linearized Gibbs-Thomson equation: $P_e = P_0(1 + 2\gamma\Omega/(k_B T R))$, where P_0 represents the equilibrium vapor pressure at a flat interface, Ω is the atomic volume, γ is the solid-vapor surface energy, k_B Boltzmann's constant, and T is the temperature.

To determine the contribution of mass transport on the degradation of the nanoparticles a mean-field model was defined using a quasi-stationary solution to the diffusion equation. Using boundary conditions based on the Gibbs-Thomson equation for the concentration of gold at the contact line of the particle-support interface, C_e, and a uniform surface concentration far away from the particle, C_∞, the growth rate by diffusion is

$$\frac{dV_{diffusion}}{dt} = \frac{2\pi\Omega r_p D}{\xi}\frac{K_1\left(r_p/\xi\right)}{K_0\left(r_p/\xi\right)}\left(C_\infty - C_e - \frac{\Gamma}{r_p}\right) \tag{2}$$

as a function of the radius of the contact circle between the particle and support, $r_p = R\sin(\theta)$. $\Gamma = A_0\Omega\gamma/k_BT$ defines the capillary length and areal density of adatoms (A_0). K_1 and K_0 are the modified Bessel functions of the second kind of order one and zero respectively, and the screening length, $\xi = (D/Q)^{1/2}$ is a characteristic distance from the particle-support interface for which the mean field concentration is reached with evaporation rate Q, and diffusion coefficient, D.

Finally, we apply assumptions to the model based on our experimental conditions. Namely, as the experiment occurs under vacuum we assume that $P << P_e$ so that evaporation always results in a decrease in free energy (standard vacuum level in the TEM column is on the order of 1×10^{-5} Pa). After applying these simplifications we come to the final model which was used to understand experimental data (expressed in terms of particle radius R, and where α and β represent the volume and surface area, respectively, of a truncated sphere with contact angle θ):

$$\frac{dR}{dt} = \frac{2\pi\Omega\sin(\theta)D}{3\alpha\xi R}\frac{K_1\left(r_p/\xi\right)}{K_0\left(r_p/\xi\right)}\left(C_\infty - C_e - \frac{\Gamma}{R}\right) - \frac{M\beta}{3\alpha}P_0(1+\frac{2\gamma\Omega}{k_bTR}). \tag{3}$$

Our analysis of experimental data, implementing automated image analysis to greatly increase the available data from an *in situ* image set, allows us to simultaneously consider growth rates of hundreds of particles to derive physically meaningful values for the parameters $D, P_0, \gamma, \theta, \xi, \Gamma$ and $C_\infty - C_e$. Particle size as a function of time for each particle was fit to a polynomial spline to aid in numerical differentiation so that the rate of change, dR/dt can be examined as a function of R. This data was then fit to our model using a simple least-squares fitting algorithm. Minimal parameter constraints based on physical intuition were applied to ensure convergence to meaningful values (constraints are listed in Supplemental Table 1). Statistical optimization using a manual parameter grid search was used to optimize initialization values while minimizing the rigidity of constraints to avoid biasing parameter values. Python scripts used in the processing and analysis are available via github.[27]

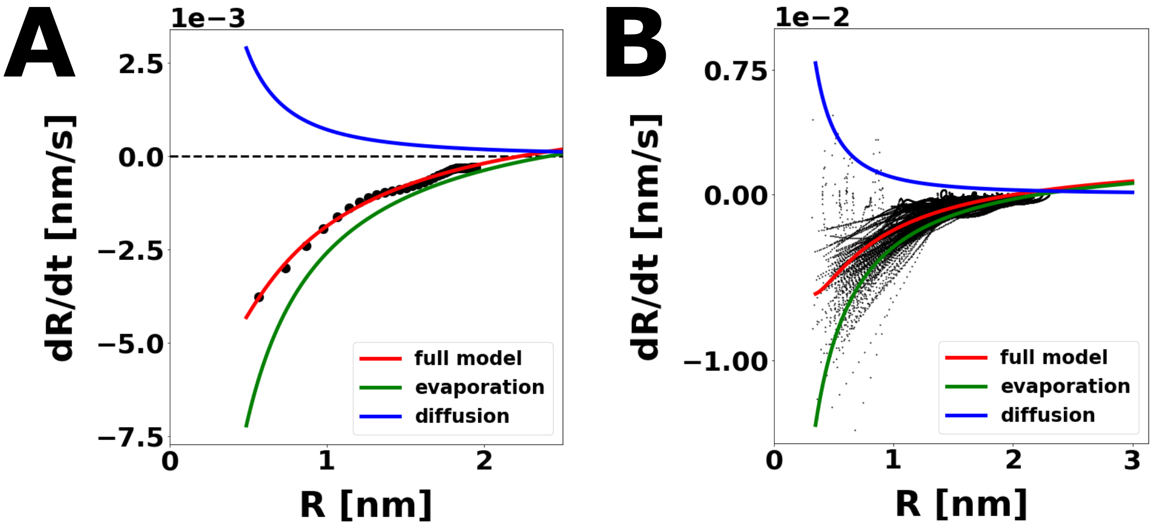

Figure 3: Equation 3 can be fit to the growth rate of individual particles, or all particles in the system. A.) shows evaporation and diffusion contributions based on the behavior of a single particle. In (B), colored lines show mean parameter fits, and their comparison to all particle timelines in the experiment, where the colored lines show mean parameter values for the system. Extracted parameter values from these fits allow characterization of the system with statistical confidence.

We find excellent agreement between experimental data and this model, as shown in Figure 3A which demonstrates how our model is able to capture the unique behavior of an individual particle. (Supplemental Figure 2 shows other examples of fits for randomly selected particles) Further, Figure 3B shows the result of fitting our model to all experimental data points; the red, blue, and green line show the average behavior extracted from mean parameter values. With the immense amount of data extracted from experiment, we are able to measure parameter values with statistical confidence and separately observe the impact of each growth mechanism. Histograms of measured parameter values found by fitting experimental data to our model can be found in Supplemental Figure 3. After removing outliers (by measuring median absolute deviation for each parameter and using a modified z-score threshold of 3.5) these parameter histograms appeared normally distributed around a mean value (Supplemental Figure 4). As shown in Table 1, our estimation of the diffusion coefficient for adatoms on the support, the solid-vapor surface energy, contact angle (measured experimentally, Supplemental Figure 5), and vapor pressure closely match values either measured experimentally or found in the literature providing validation for our model and data extraction method.

Table 1: Comparison between parameter values obtained from fitting our model to values found in experiment or in the literature.

Parameter	Fit Value	Reference Value
D	$2.7 \times 10^3 \frac{nm^2}{s}$	$3.8 \times 10^5 \frac{nm^2}{s}$[28]
P_0	$1.68 \times 10^{-5} Pa$	$4.9 \times 10^{-4} Pa$[29]
γ	$1.51 \frac{J}{m^2}$	$1.5 \frac{J}{m^2}$[30]
θ	$115 - 131°$	$120 \pm 5°$

Established research has studied the impact of surface effects on properties of materials, and shown that at the smallest scales the surface energy of many materials is expected to be larger than that of the corresponding bulk materials.[23] Moreover, studies have provided a theoretical understanding of how the high surface energy of small particles can accelerate the shrinking of particles.[31,32] We find that the vapor pressure at the particle surface, determined by P_0 for bulk interfaces and modified by γ according to the Gibbs-Thomson equation, is clearly captured by our model. In agreement with other research, we contend that the dominant size-dependency of particle growth comes from the difference between the vapor pressure at the particle surface and the surrounding environment.[33,34]

Figure 4 demonstrates the strong size-dependence on evaporation seen in our system, as particle size alone serves as an accurate predictor of evaporation. Visualization of experimental data (Figure 1E, for example) shows that false positives (particles which were expected to evaporate but did not) would have evaporated if the experiment had continued. Interestingly, $R = 1.5$ nm, which predicts evaporation, corresponds closely with the mean particle radius at the end of the experiment (dark red in Figue 1C) and the radius for which the evaporation rate approaches 0 (Figure 3). Further analysis (Supplemental Figure 6) suggests that this final particle size is stable and does not change significantly with time.

In addition to providing reliable estimates of physical parameters based on high-resolution time resolved measurements, another major benefit to our data-rich approach to analyzing *in situ* data is that it allows us to quantitatively compare the behavior of neighboring particles

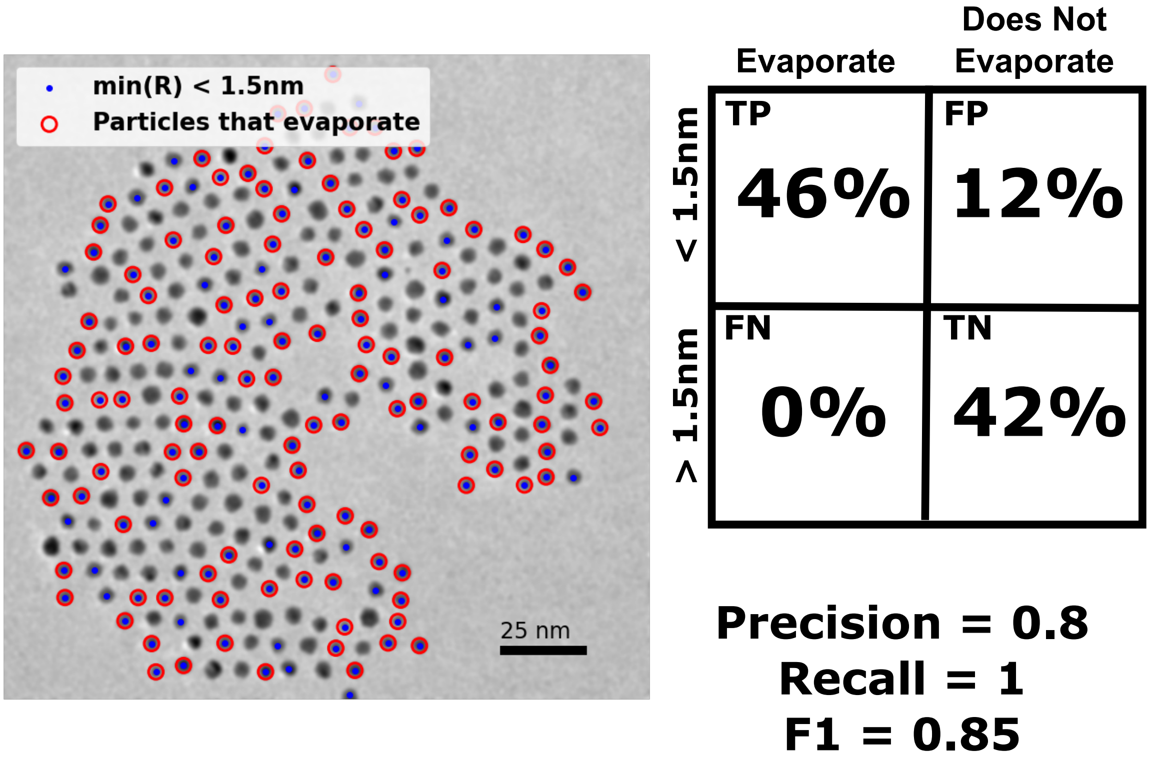

Figure 4: Particle size serves as a predictor for evaporation. Particles which reach a radius $\leq$ 1.5 nm eventually evaporate. A confusion matrix, and standard accuracy metrics are shown. High precision indicates few false positives, high recall indicates a high detection rate, and F1 score gives general accuracy as a mean of precision and recall. TP, FP, FN, and TN stand for true positive, false positive, false negative and true negative, respectively.

and observe actual diffusional interactions between particles (Figure 5A and B). Comparison between our model and the experimental data shows the small, but non-negligible, impact of mass transport through surface diffusion on the growth rate of supported nanoparticles which would be impossible to observe without using advanced data extraction techniques. With validation from the other parameters of our model, for which we have expected values from the literature and experiment, we can characterize the mean-field concentration gradient at the particle-support interface. Our data indicate that, on average, there is a net flux of mass into the particle causing growth from a small concentration of adsorbed gold on the support. Again comparing to Figure 5B, where the green particle clearly grows as a result of additional mass from its neighbors, this is justified. The concentration gradient on the support should also be considered with respect to the method for nanoparticle deposition. As particles were synthesized *ex situ* and then drop-cast onto the surface we expect that very little gold will be adsorbed on the support away from a particle. Therefore, the nearly-zero concentration of gold adatoms on the support is not surprising. We expect that any adsorbed gold atoms which contribute to diffusion are left behind during the final stages of evaporation. Correspondingly, since diffusion fields are closely tied to evaporation events, adatoms contribute most strongly to local diffusion and do not develop into a uniform mean-field concentration. This is consistent with the growth trends shown in Figure 5 (individual fits presented in Supplemental Figure 7 and Supplemental Table 2). Though the concentration gradient near all particles is found to be similar and in agreement with the mean value ($+5\times10^{-4} - 1\times10^{-3}[atoms/nm^2]$), the capillary lengths (Γ) for the red and blue particles are orders of magnitude larger than that of the green particle. This trend continues when applied to all measured particles (bottom two rows of Supplemental Table 2), where we find that capillary lengths of evaporating particles are larger than those of non-evaporating particles by a statistically significant margin ($p = 0.0005$). This confirms our understanding of concentration gradients driven by high interfacial concentrations at small particles due to the Gibbs-Thomson Effect. Moreover, we can see the impact of particle size on diffusion behavior by observing the diffusion component of the growth rate for shrinking particles. There is clearly a critical radius at which capillary effects overcome the positive concentration gradient and cause small particles to rapidly shrink (Supplemental Figure 7). Though a mean-field model cannot be expected to describe the evolution of individual particles in detail, our ability to compare the behavior of many different particles in unique conditions allows us to reconcile intuitive physical models with random nanoscale fluctuations, and to understand the origin of unexpected behaviors.

Applied experiments have clearly shown the impact of particle spacing on catalytic activity and stability of supported metal catalysts.[35,36] Research has given conflicting reports on whether particle spacing positively or negatively affects performance and stability.[37] Electrostatic shielding, which leads to a modified reaction potential, of close-packed particles

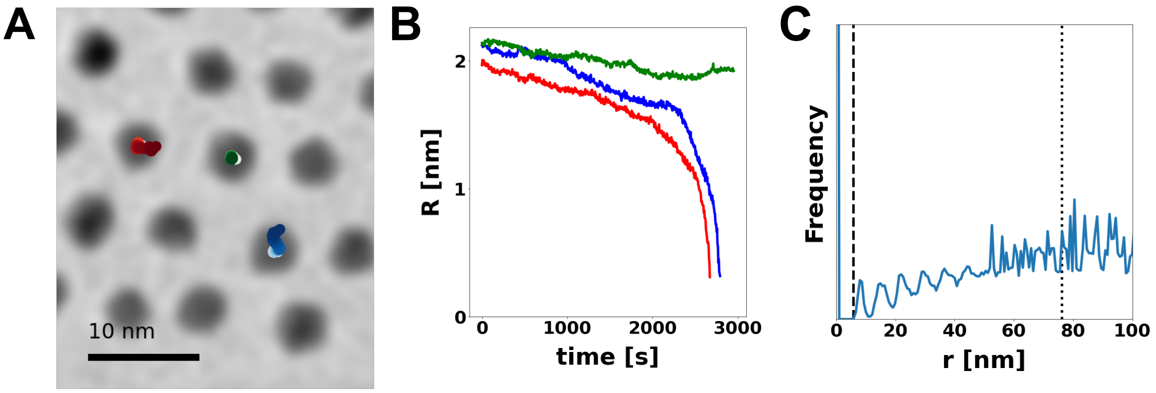

Figure 5: Additional analysis shows unique interactions between particles. A.) shows how the center of mass of three neighboring particles shift with time (colors darken as time progresses). The same color scheme is used in B.) to show particle radii change. A calculated radial distribution function for particle centers in the first frame of the experiment is shown in C.) to display the distances between neighboring particles. The dashed line corresponds to the mode of the fit screening length, while the dotted line shows the overall mean.

has been suggested as the reason for exceptionally high catalytic activity for supported Pt nanoparticles in fuel cell membranes.[38] Additionally, it is well known that particle loading, especially for very small particles, leads to instability and catalyst degradation by Ostwald ripening or particle migration and coalescence.[39,40] Still, fundamental mechanisms for interaction between supported particles, and the influence of particle spacing are not well studied, and available results depend strongly on the specific conditions of the experiment or theory. One approach for estimating the interaction between supported particles relies on solving the diffusion equation for a basis of randomly spaced particles which can be translated in space to approximate an infinite system of randomly distributed particles. Analytical results can be obtained for small systems of just two particles to describe the diffusional interactions between particles, and systems of large particles can be solved numerically to elucidate the impact of longer range interactions.[41,42] These theoretical results suggest that particle interactions are not limited to nearest-neighbors, and that even interactions between particles in different basis cells can be quantified to show divergence from mean-field depictions. Though our model describes the interaction of a single particle with a mean-field concentration, we can use the screening length, ξ, derived from our model to characterize the length over which particles interact. In contrast to all other parameters, for which fit values are normally-distributed such that outlying parameter values could be attributed to numerical errors in the fitting code, model fits for ξ exhibited a mode of 5.7 nm, and a broad distribution of measurements at larger values (mean of 76.1nm, see Supplemental Figures 3 and 4). Interestingly, these values closely correspond with physically meaningful distances in the experimental system. As shown in Figure 5C, the short distance (dashed line) closely approximates the nearest-neighbor distance for periodically arranged nanoparticles. Alternatively, the larger distance (dotted line in Figure 5C) coincides with the distance over which the array of nanoparticles becomes considerably disordered. Here, where self-assembly allows nanoparticles to assume a periodic arrangement, this distance is on the order of the size of the isolated group of nanoparticles shown in Figure 1A. Based on these correlations we interpret the data to show that diffusional interactions, overall, are strongest between neighboring particles and that growth by diffusion is coupled with the evaporation of nearby particles. Still, as evidenced by the secondary value of ξ and as proposed in theory, long range interactions contribute significantly to the global evolution of the evaporating nanoparticles.

In summary, we demonstrate a method for detailed quantification of data collected using *in situ* TEM. Aided by unsupervised machine learning, positions and size of hundreds of particles are extracted as a function of time to yield an experimental description of a dynamically evolving system of a model supported catalyst. After developing a model to understand the competition between evaporation and surface diffusion, statistically-validated parameter values were extracted to verify our understanding of the physics behind particle growth, and characterize the system in terms of variables such as local concentration gradients and screening lengths which are impossible to directly measure in experiment. We discuss the applicability of mean-field models to capture dynamic changes in nanoscale systems, and show that, with the help of modern data analysis, deviations from our theoretical understanding can be attributed to local changes in the system. Using our method, we quantify the interaction distance in an array of supported nanoparticles to elucidate how surface diffusion impacts particle growth over a variety of length scales.

Supporting Information

Supplemental Figures 1-7

Supplemental Tables 1 and 2

Acknowledgements

J.P.H and E.A.S acknowledge support through the National Science Foundation, Division of Materials Research, Metals and Metallic Nanostructures Program under Grant 1809398. This research used resources of the Center for Functional Nanomaterials, which is a U.S. DOE Office of Science Facility, at Brookhaven National Laboratory under Contract No. DE-SC00127044. P.W.V. acknowledges financial assistance under award 70NANB19H005 from U.S. Department of Commerce, National Institute of Standards and Technology as part of the Center for Hierarchical Materials Design. We would like to thank Dmitri Zakharov and Kim Kisslinger of the Center for Functional Nanomaterials for assisting with experiments, Katherine Elbert and Christopher Murray from the University of Pennsylvania Department of Chemistry for help with nanoparticle synthesis and self-assembly.

References

(1) Liu, L.; Corma, A. Metal Catalysts for Heterogeneous Catalysis: From Single Atoms to Nanoclusters and Nanoparticles. *Chem. Rev.* **2018**, *118*, 4981–5079.

(2) Wynblatt, P.; Gjostein, N. SUPPORTED METAL CRYSTALLITES. *Prog. Solid State Chem.* **1975**, *9*, 21–58.

(3) Lifshitz, I.; Slyozov, V. The kinetics of precipitation from supersaturated solid solutions. *J. Phys. Chem. Solids* **1961**, *19*, 35–50.

(4) Voorhees, P. W. The theory of Ostwald ripening. *J. Stat. Phys.* **1985**, *38*, 231–252.

(5) Hu, S. L.; Li, W. X. Metal-support interaction controlled migration and coalescence of supported particles. *Sci. China Technol. Sci.* **2019**, *62*, 762–772.

(6) Snyder, V. A.; Alkemper, J.; Voorhees, P. W. Transient Ostwald ripening and the disagreement between steady-state coarsening theory and experiment. *Acta Mater.* **2001**, *49*, 699–709.

(7) Zhdanov, V. P.; Larsson, E. M.; Langhammer, C. Novel aspects of Ostwald ripening of supported metal nanoparticles. *Chem. Phys. Lett.* **2012**, *533*, 65–69.

(8) Heinemann, K.; Poppa, H. Direct observation of small cluster mobility and ripening. *Thin Solid Films* **1976**, *32*, 276.

(9) Taheri, M. L.; Stach, E. A.; Arslan, I.; Crozier, P. A.; Kabius, B. C.; LaGrange, T.; Minor, A. M.; Takeda, S.; Tanase, M.; Wagner, J. B.; Sharma, R. Current status and future directions for in situ transmission electron microscopy. *Ultramicroscopy* **2016**, *170*, 86–95.

(10) Zhang, C.; Han, R.; Zhang, A. R.; Voyles, P. M. Denoising atomic resolution 4D scanning transmission electron microscopy data with tensor singular value decomposition. *Ultramicroscopy* **2020**, *219*, 113123.

(11) Li, W.; Field, K. G.; Morgan, D. Automated defect analysis in electron microscopic images. *npj Comput. Mater.* **2018**, *4*, 1–9.

(12) Ziatdinov, M.; Dyck, O.; Maksov, A.; Li, X.; Sang, X.; Xiao, K.; Unocic, R. R.; Vasudevan, R.; Jesse, S.; Kalinin, S. V. Deep Learning of Atomically Resolved Scanning

Transmission Electron Microscopy Images: Chemical Identification and Tracking Local Transformations. *ACS Nano* **2017**, *11*, 12742–12752.

(13) Madsen, J.; Liu, P.; Kling, J.; Wagner, J. B.; Hansen, T. W.; Winther, O.; Schiøtz, J. A deep learning approach to identify local structures in atomic-resolution transmission electron microscopy images. *Adv. Theory Simulations* **2018**, *1*, 1800037.

(14) Elbert, K. C.; Jishkariani, D.; Wu, Y.; Lee, J. D.; Donnio, B.; Murray, C. B. Design, Self-Assembly, and Switchable Wettability in Hydrophobic, Hydrophilic, and Janus Dendritic Ligand-Gold Nanoparticle Hybrid Materials. *Chem. Mater.* **2017**, *29*, 8737–8746.

(15) Jishkariani, D.; Elbert, K. C.; Wu, Y.; Lee, J. D.; Hermes, M.; Wang, D.; Van Blaaderen, A.; Murray, C. B. Nanocrystal Core Size and Shape Substitutional Doping and Underlying Crystalline Order in Nanocrystal Superlattices. *ACS Nano* **2019**, *13*, 5712–5719.

(16) DensSolutions, Wildfire In Situ Heating. `https://denssolutions.com/products/wildfire/`.

(17) Ristau, R.; Clasen, P.; Gorskowki, E.; Harmer, M.; Kiely, C.; Hussain, I.; Brust, M. Electron microscopy studies of the thermal stability of gold nanoparticle arrays. *Gold Bull.* **2009**, *42*, 133–143.

(18) Cortie, M. B.; Coutts, M. J.; Ton-That, C.; Dowd, A.; Keast, V. J.; McDonagh, A. M. On the coalescence of nanoparticulate gold sinter ink. *J. Phys. Chem. C* **2013**, *117*, 11377–11384.

(19) Horwath, J. P.; Zakharov, D. N.; Megret, R.; Stach, E. A. Understanding important features of deep learning models for segmentation of high-resolution transmission electron microscopy images. *npj Comput. Mater.* **2020**, *108*, 1–9.

(20) Vyas, L.; Horwath, J. P.; Stach, E. A. Tutorial on Unsupervised Image Segmentation for Electron Microscopy. https://mlforem.github.io/, 2021.

(21) Paszke, A.; Gross, S.; Chintala, S.; Chanan, G.; Yang, E.; DeVito, Z.; Lin, Z.; Desmaison, A.; Antiga, L.; Lerer, A. Automatic differentiation in PyTorch. *NIPS 2017* **2017**,

(22) van der Walt, S.; Schoenberger, J. L.; Nunes-Iglesias, J.; Boulogne, F.; Warner, J. D.; Yager, N.; Gouillart, E.; Yu, T. scikit-image: image processing in Python. *PeerJ* **2014**, *2*, 435.

(23) Blackman, M.; Lisgarten, N.; Skinner, L. Surface Energy and Evaporation Rate of Spherical Particles of Radii less than 500 A. *Nature* **1968**, *217*, 1245–1246.

(24) Nanda, K. K. Bulk cohesive energy and surface tension from the size-dependent evaporation study of nanoparticles. *Appl. Phys. Lett.* **2005**, *87*, 43–46.

(25) Meng, A. C.; Low, K.-b.; Foucher, A. C.; Li, Y.; Petrovic, I.; Stach, E. Anomalous Metal Vaporization from Pt / Pd / Al2O3 Under Redox Conditions. *ChemRxiv Prepr.* **2020**, DOI: https://doi.org/10.26434/chemrxiv.13087574.v1, accessed 2021-05-11.

(26) Safarian, J.; Engh, T. A. Vacuum evaporation of pure metals. *Metall. Mater. Trans. A Phys. Metall. Mater. Sci.* **2013**, *44*, 747–753.

(27) Horwath, J. Competitive Growth. https://github.com/jhorwath/CompetitiveGrowth, 2021.

(28) Ruffino, F.; Cacciato, G.; Grimaldi, M. G. Surface diffusion coefficient of Au atoms on single layer graphene grown on Cu. *J. Appl. Phys.* **2014**, *115*.

(29) Alcock, C. B.; Itkin, V. P.; Horrigan, M. K. Vapour Pressure Equations for the Metallic Elements: 298–2500K. *Canadian Metallurgical Quarterly* **1984**, *23*, 309–313.

(30) Aqra, F.; Ayyad, A. Surface energies of metals in both liquid and solid states. *Appl. Surf. Sci.* **2011**, *257*, 6372–6379.

(31) Mullins, W. W.; Rohrer, G. S. Nucleation Barrier for Volume-Conserving Shape Changes of Faceted Crystals. *J. Am. Ceram. Soc.* **2000**, *16*, 214–216.

(32) Somorjai, G. A. Surface Energy Effect on Diffusion- Controlled Particle Growth. *J. Chem. Phys.* **1961**, *655*.

(33) Couchman, P.; Jesser, W. Thermodynamic theory of size dependence. *Nature* **1977**, *269*, 481–483.

(34) Nanda, K. K.; Kruis, F. E.; Fissan, H. Evaporation of Free PbS Nanoparticles: Evidence of the Kelvin Effect. *Phys. Rev. Lett.* **2002**, *89*, 1–4.

(35) Karim, W.; Spreafico, C.; Kleibert, A.; Gobrecht, J.; Vandevondele, J.; Ekinci, Y.; Bokhoven, J. A. V. Catalyst support effects on hydrogen spillover. *Nature* **2017**, *541*, 68–71.

(36) Speder, J.; Altmann, L.; Baumer, M.; Kirkensgaard, J.; Mortensen, K.; Arenz, M. The particle proximity effect: from model to high surface area fuel cell catalyst. *RSC Adv.* **2014**, *4*, 14971–14978.

(37) Antolini, E. Structural parameters of supported fuel cell catalysts : The effect of particle size , inter-particle distance and metal loading on catalytic activity and fuel cell performance. *Appl. Catal. B, Environ.* **2016**, *181*, 298–313.

(38) Nesselberger, M.; Roefzaad, M.; Hamou, R. F.; Biedermann, P. U.; Schweinberger, F. F.; Kunz, S.; Schloegl, K.; Wiberg, G. K. H.; Ashton, S.; Heiz, U.; Mayrhofer, K. J. J.; Arenz, M. The effect of particle proximity on the oxygen reduction rate of size-selected platinum clusters. *Nat. Mater.* **2013**, *12*, 919–924.

(39) Hansen, T. W.; Delariva, A. T.; Challa, S. R.; Datye, A. K. Sintering of catalytic nanoparticles: Particle migration or ostwald ripening? *Acc. Chem. Res.* **2013**, *46*, 1720–1730.

(40) Simonsen, S. B.; Chorkendorff, I.; Dahl, S.; Skoglundh, M.; Sehested, J.; Helveg, S. Direct Observations of Oxygen-induced Platinum Nanoparticle Ripening Studied by In Situ TEM. *J. Am. Chem. Soc.* **2010**, *132*, 7968–7975.

(41) Voorhees, P. W.; Glicksman, M. E. Solution to the multi-particle diffusion problem with applications to Ostwald ripening-I. Theory. *Acta Metall.* **1984**, *32*, 2001–2011.

(42) Dadyburjor, D. B.; Marsh, S. P.; Glicksman, M. E. The role of multiparticle-adatom interactions on the sintering of supported metal catalysts. *J. Catal.* **1986**, *99*, 358–374.

Quantifying Competitive Growth Processes in Supported Nanocatalyst Systems:

James P. Horwath[1], Peter W. Voorhees[2], Eric A. Stach[1,*]

1. University of Pennsylvania, Department of Materials Science and Engineering, Philadelphia, PA 19104
2. Northwestern University, Department of Materials Science and Engineering, Evanston, IL 60208

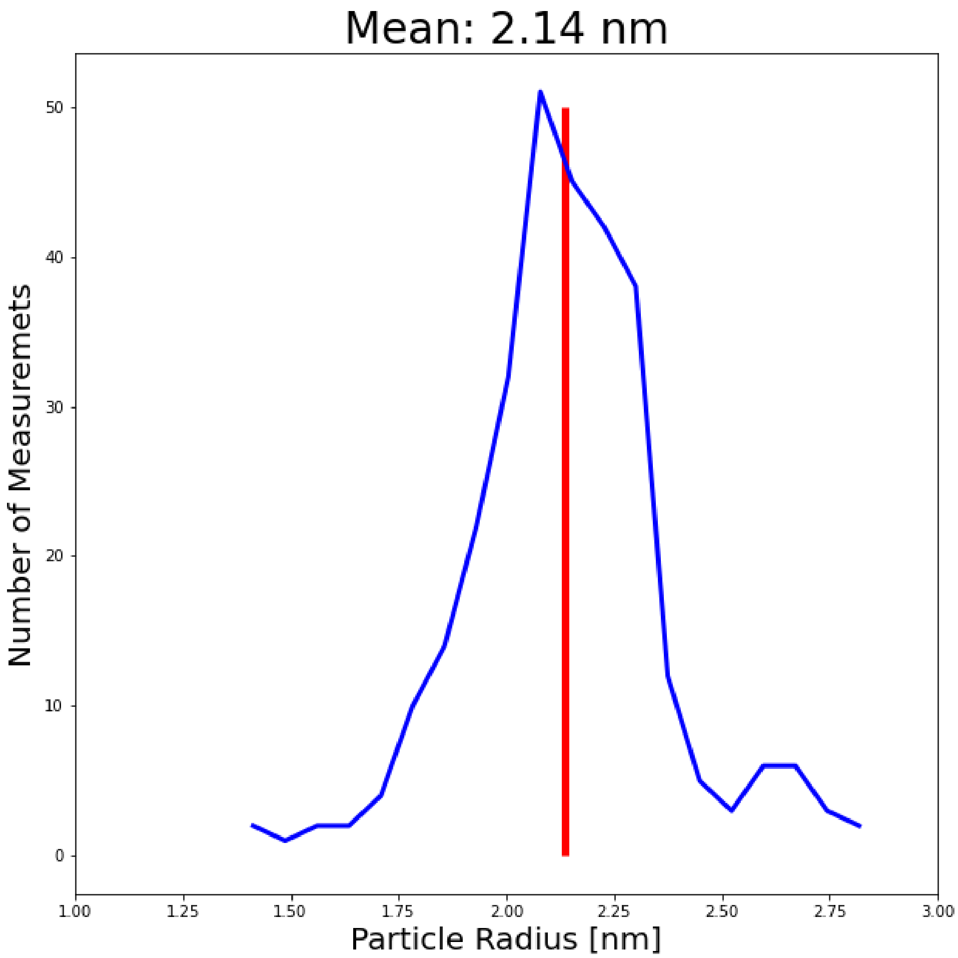

Supplemental Figure 1. Particle size distribution at t = 0. Red line and figure title show the mean particles size: R = 2.14nm

Supplemental Table 1. List of parameters and constraints used to fit experimental data to the model described in Equation 3.

Parameter	Lower Bound	Upper Bound
$A_1 = 2\pi\Omega D/3$ [nm^3/s]	0	∞
$A_2 = C_\infty - C_e$ [nm^{-2}]	$-\infty$	∞
$A_3 = \Gamma$ [nm^{-1}]	$-\infty$	0
$A_4 = MP_0/3$ [nm/s]	$-\infty$	∞
$A_5 = 2\gamma\Omega/k_BT$ [nm]	$-\infty$	∞
θ [radians]	$\pi/2$	π
ξ [nm]	0	100

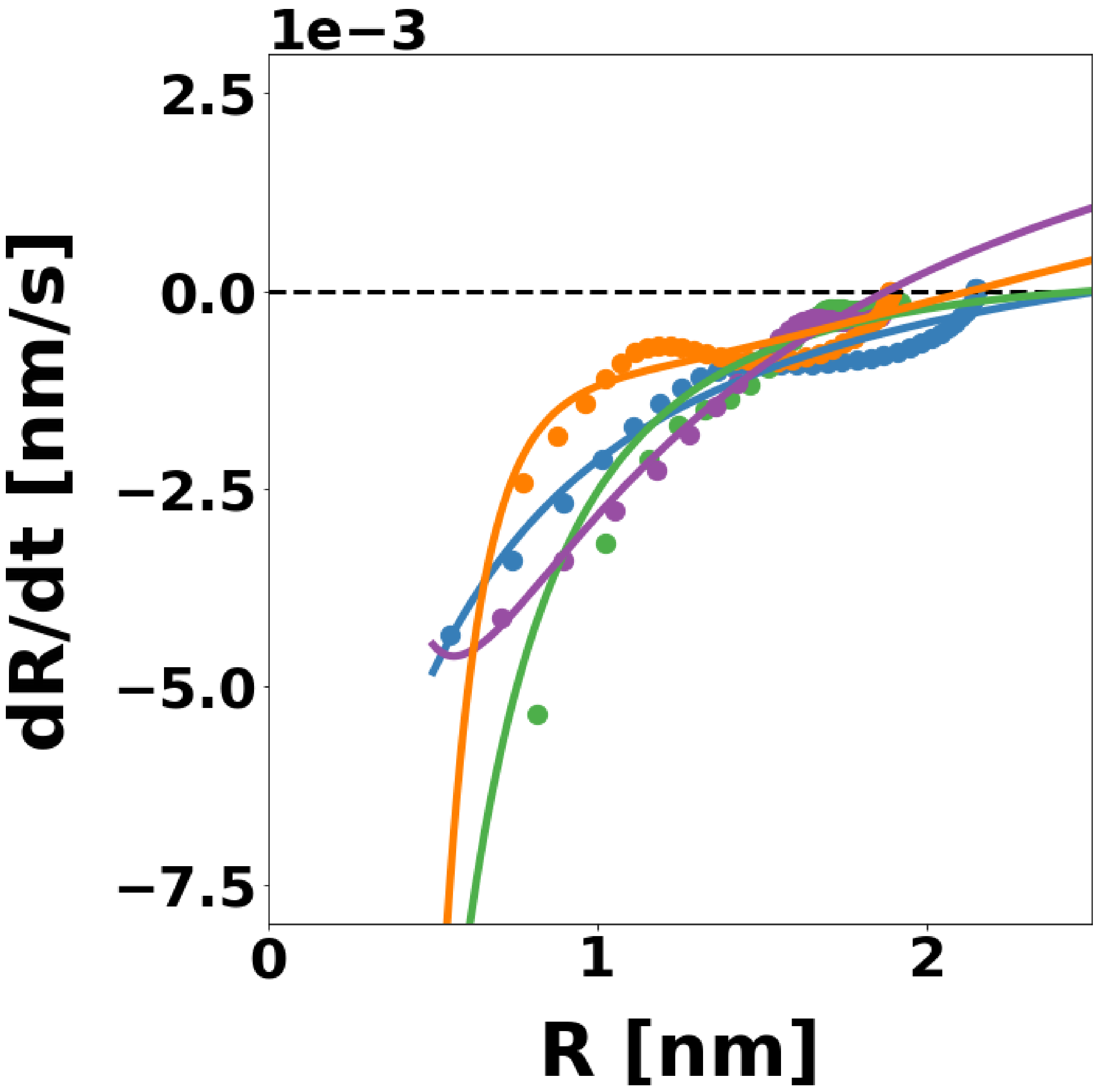

Supplemental Figure 2. Demonstration of model fits to a randomly selected set of particles. Correspondingly colored points and lines represent the experimental data and fit for an individual particle, respectively. Note the up-turn predicted by the fit at small radius in the purple particle – this is not physical and is likely a result of not having enough measurements at small R to properly represent the data.

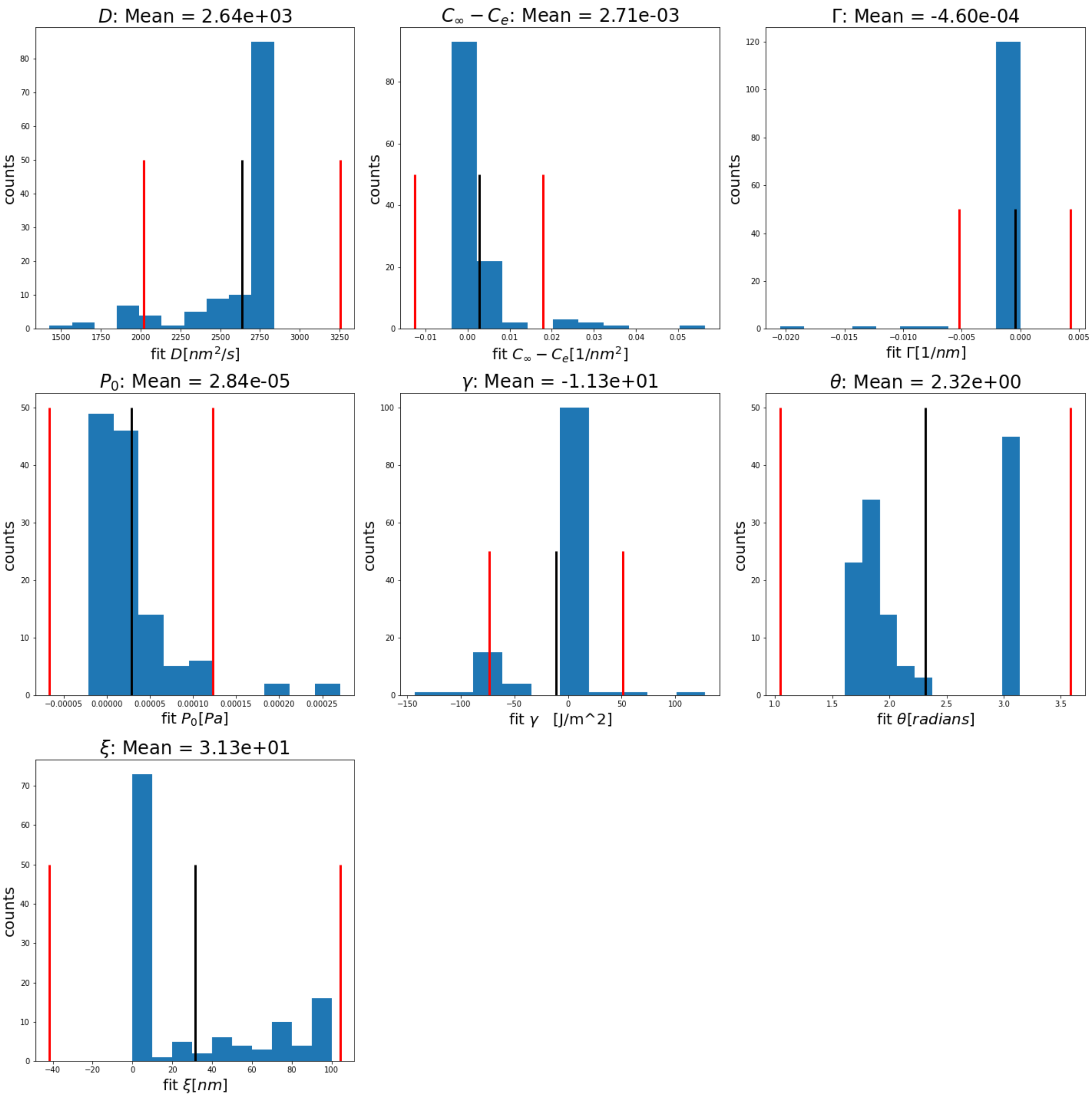

D: Mean = 2.64e+03

$C_\infty - C_e$: Mean = 2.71e-03

Γ: Mean = -4.60e-04

P_0: Mean = 2.84e-05

γ: Mean = -1.13e+01

θ: Mean = 2.32e+00

ξ: Mean = 3.13e+01

Supplemental Figure 3. Histogram of raw parameter values taken from fitting 125 particles to Equation 3.

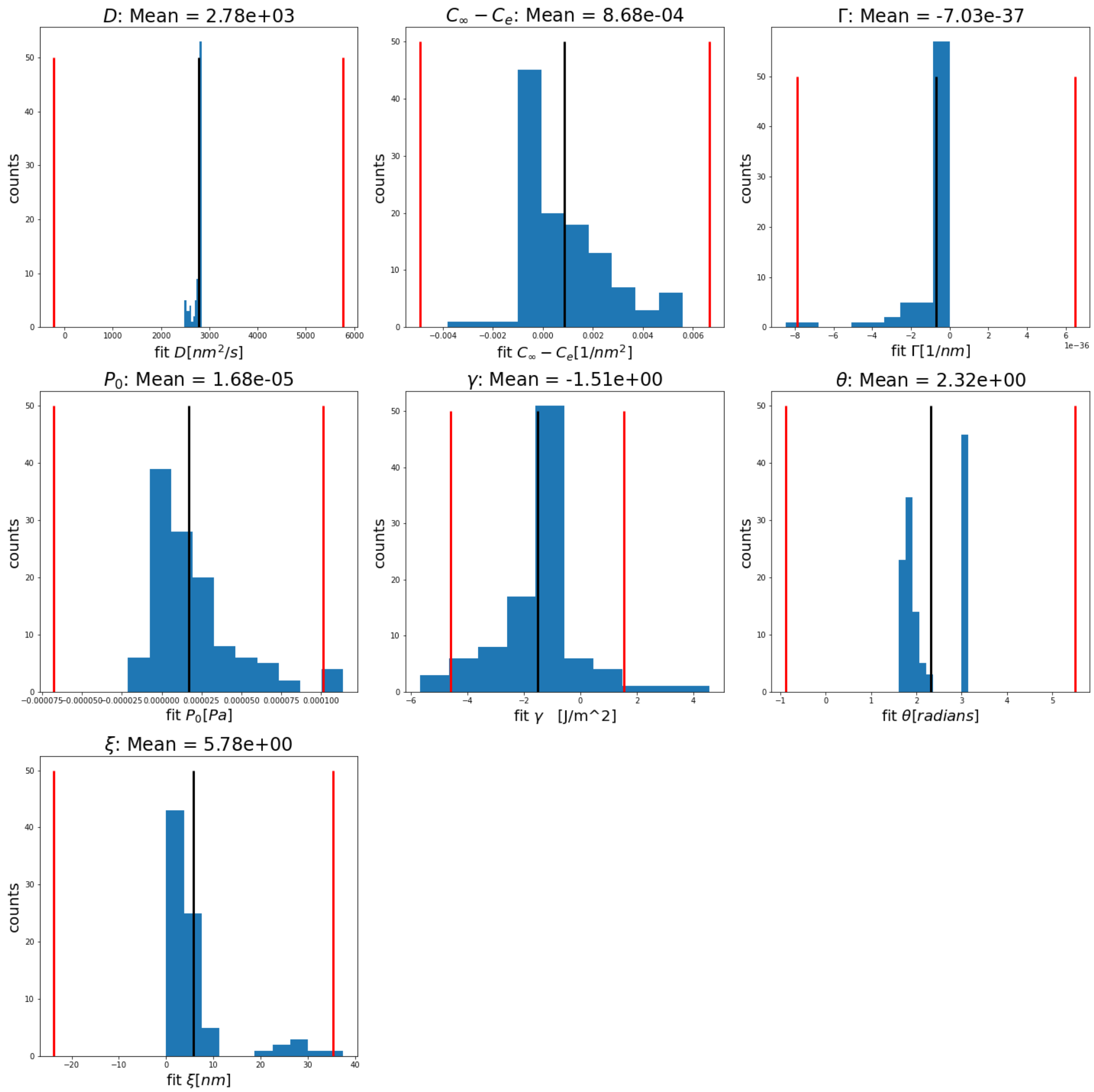

Supplemental Figure 4. Histograms of parameter values after removing outliers. Outliers were defined by calculating the median absolute deviation of each value, and then using a modified *z*-score of 3.5 as a threshold.

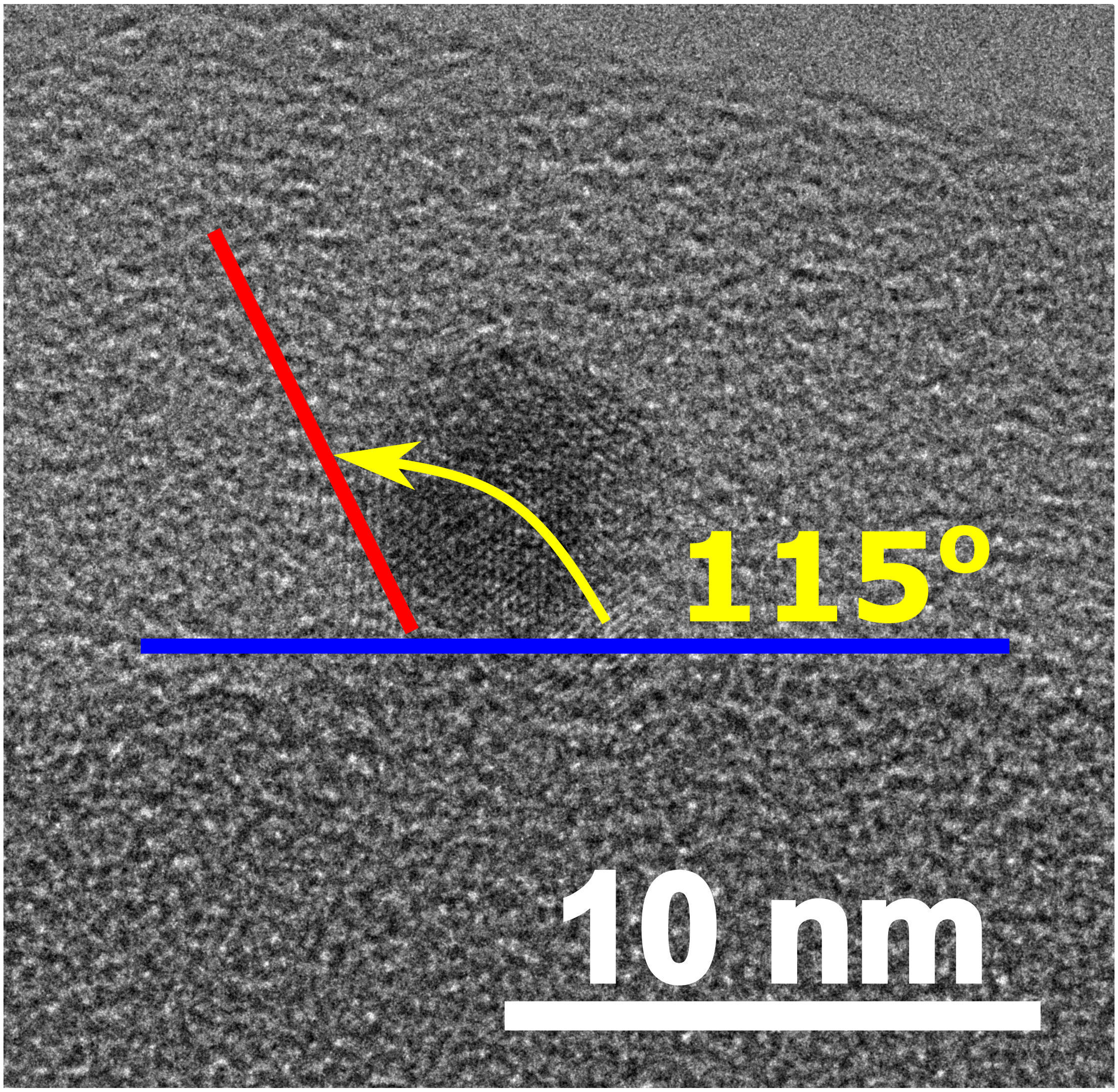

Supplemental Figure 5. Image showing the measurement of contact angle form an experimental TEM image. Gold particles were drop cast onto SiO_2 Stöber Spheres, plasma cleaned via the method described in the text, and imaged. The contact angle could be directly observed for particles deposited perpendicular to the imaging direction.

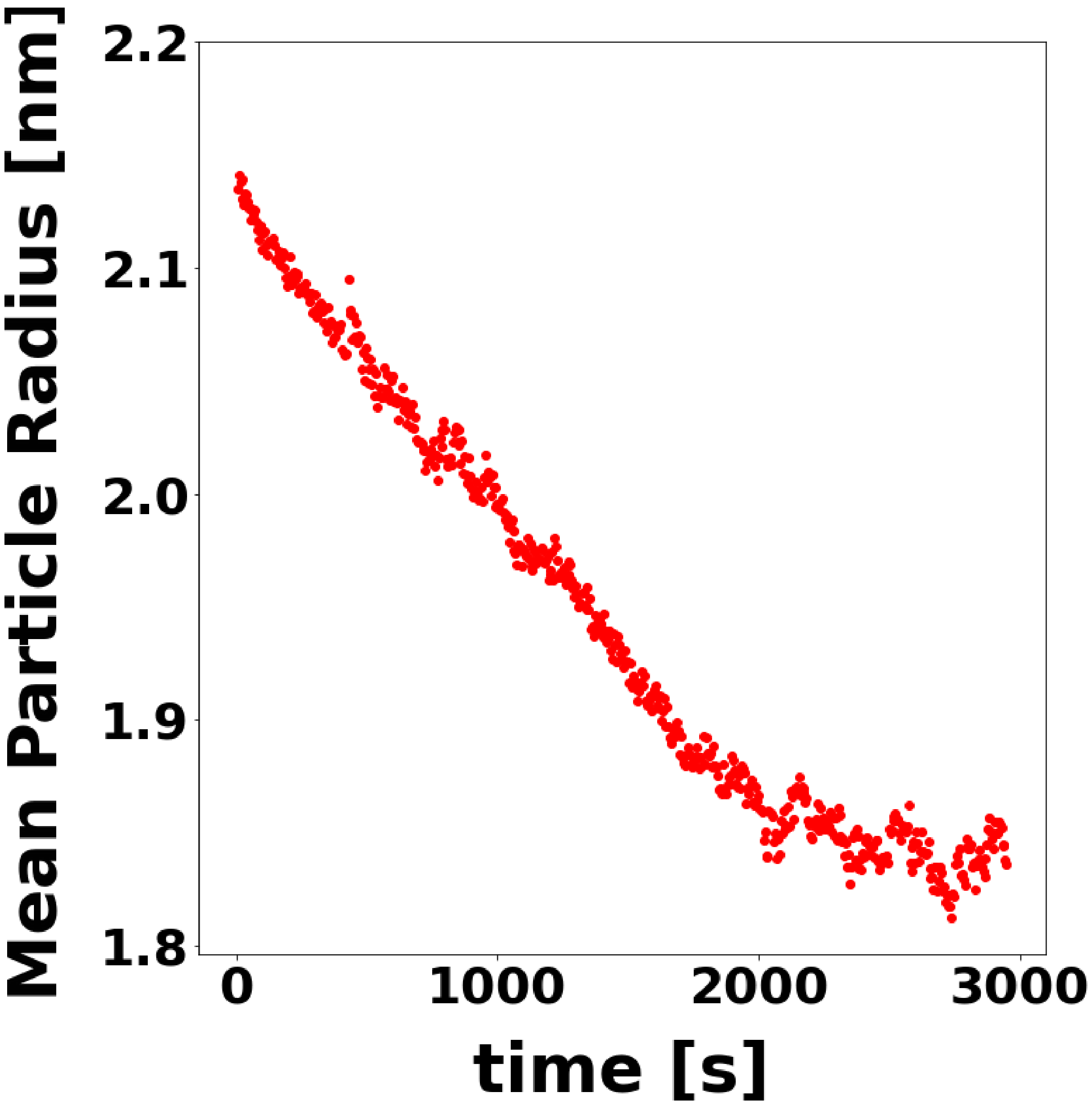

Supplemental Figure 6. Mean particle size a function of time. The plot shows that the decrease in particle size slows down as time progresses, signifying that a stable particle size is reached after a transient period of evaporation.

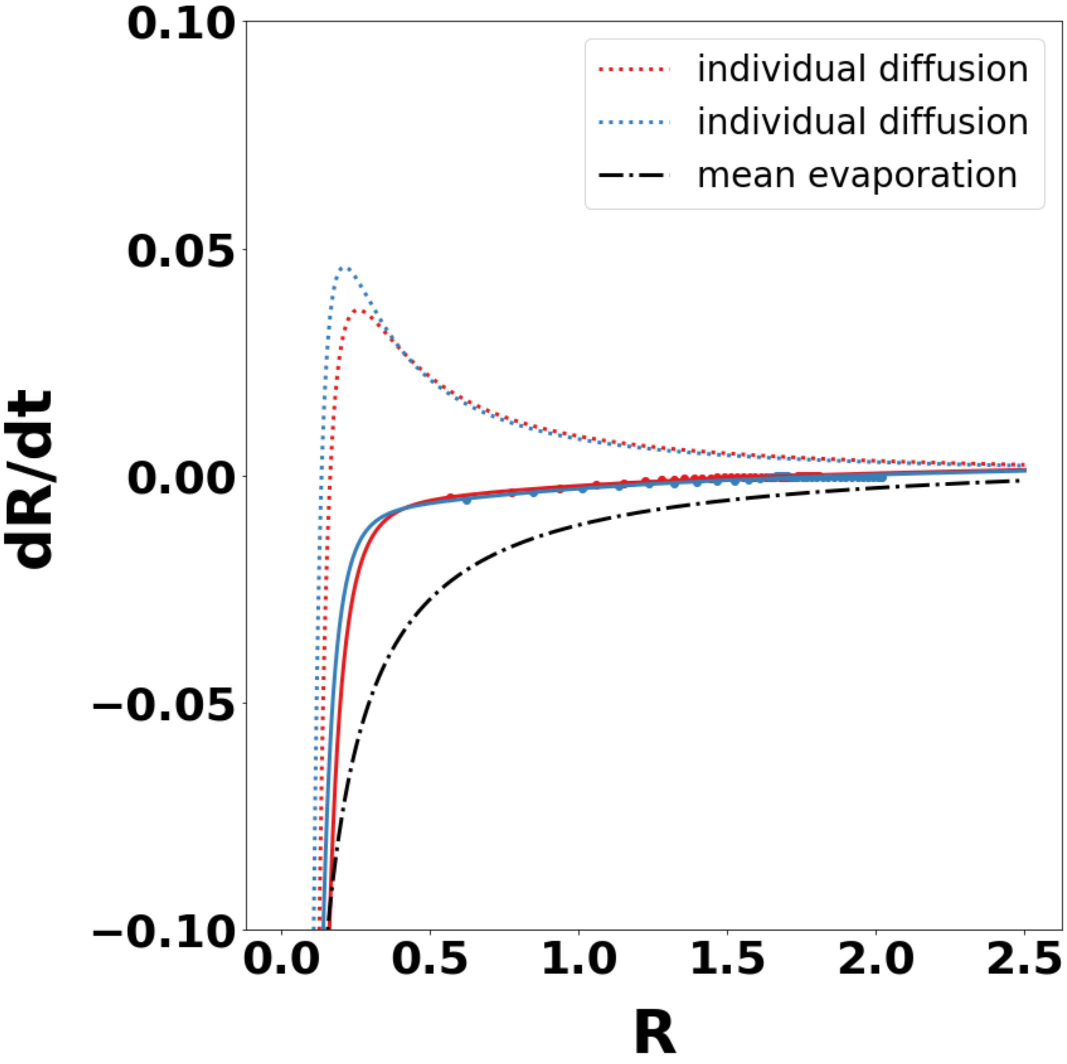

Supplemental Figure 7. Individual fits to the diffusion component of the red and blue particles in Figure 3. The diffusion curve reaches a maximum near 0.5nm. Particles larger than this grow due to the relatively large concentration of adatoms on the support. In contrast, small particles rapidly shrink as the Gibbs-Thomson effect drives their interfacial concentration to become larger than the adatom concentration.

	$C_\infty - C_e \left[\frac{1}{nm^2}\right]$	$\Gamma \left[\frac{1}{nm}\right]$
	7.6 e -4	3.6 e -9
	9.5 e -4	1.16 e -4
	8.5 e -4	8.5 e -5
All that shrink	8.7 e -4	1 e -4
Don't shrink	7 e -4	1e-6

Supplemental Table 2. Fit values for particles shown in Figure 3 of the main text. Colors correspond to the colored particles in the figure. A capillary length (Γ) for the green particle cannot be accurately calculated since it does not shrink significantly

Quantifying Competitive Growth Processes in Supported Nanocatalyst Systems:

James P. Horwath[1], Peter W. Voorhees[2], Eric A. Stach[1,*]

1. University of Pennsylvania, Department of Materials Science and Engineering, Philadelphia, PA 19104
2. Northwestern University, Department of Materials Science and Engineering, Evanston, IL 60208

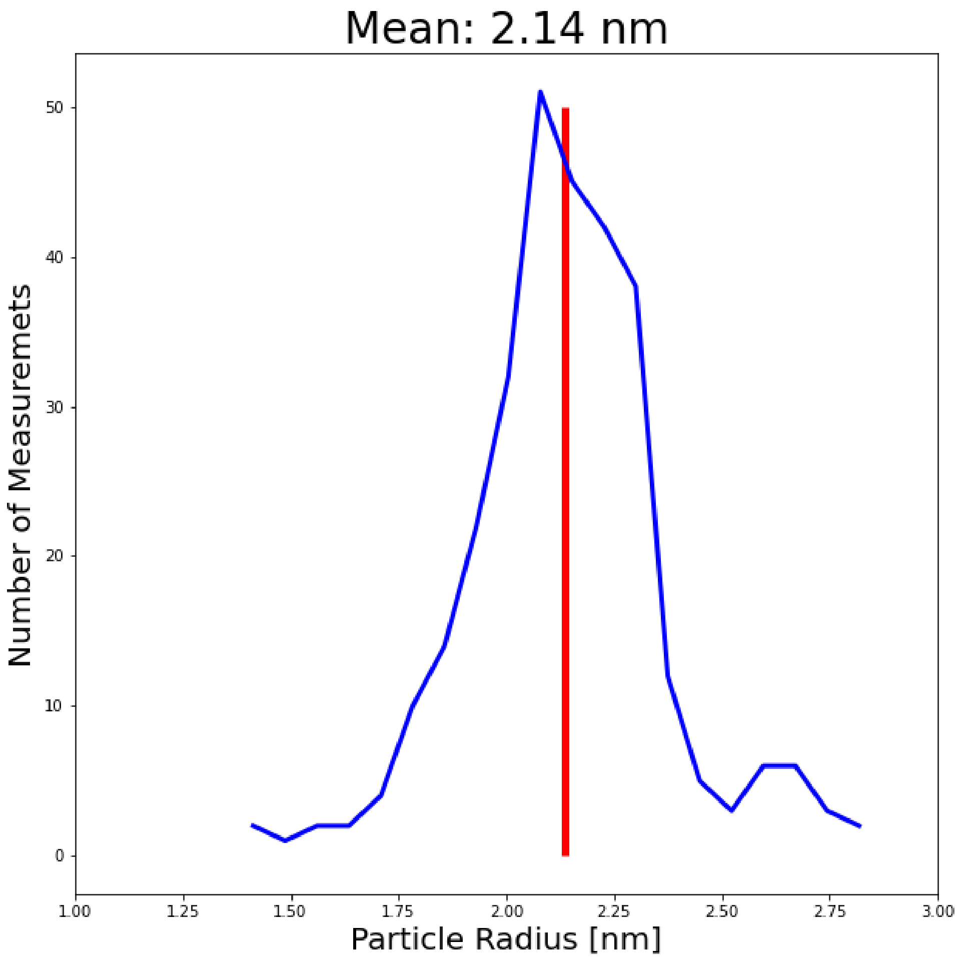

Supplemental Figure 1. Particle size distribution at t = 0. Red line and figure title show the mean particles size: R = 2.14nm

Supplemental Table 1. List of parameters and constraints used to fit experimental data to the model described in Equation 3.

Parameter	Lower Bound	Upper Bound
$A_1 = 2\pi\Omega D/3$ [nm^3/s]	0	∞
$A_2 = C_\infty - C_e$ [nm^{-2}]	$-\infty$	∞
$A_3 = \Gamma$ [nm^{-1}]	$-\infty$	0
$A_4 = MP_0/3$ [nm/s]	$-\infty$	∞
$A_5 = 2\gamma\Omega/k_BT$ [nm]	$-\infty$	∞
θ [radians]	$\pi/2$	π
ξ [nm]	0	100

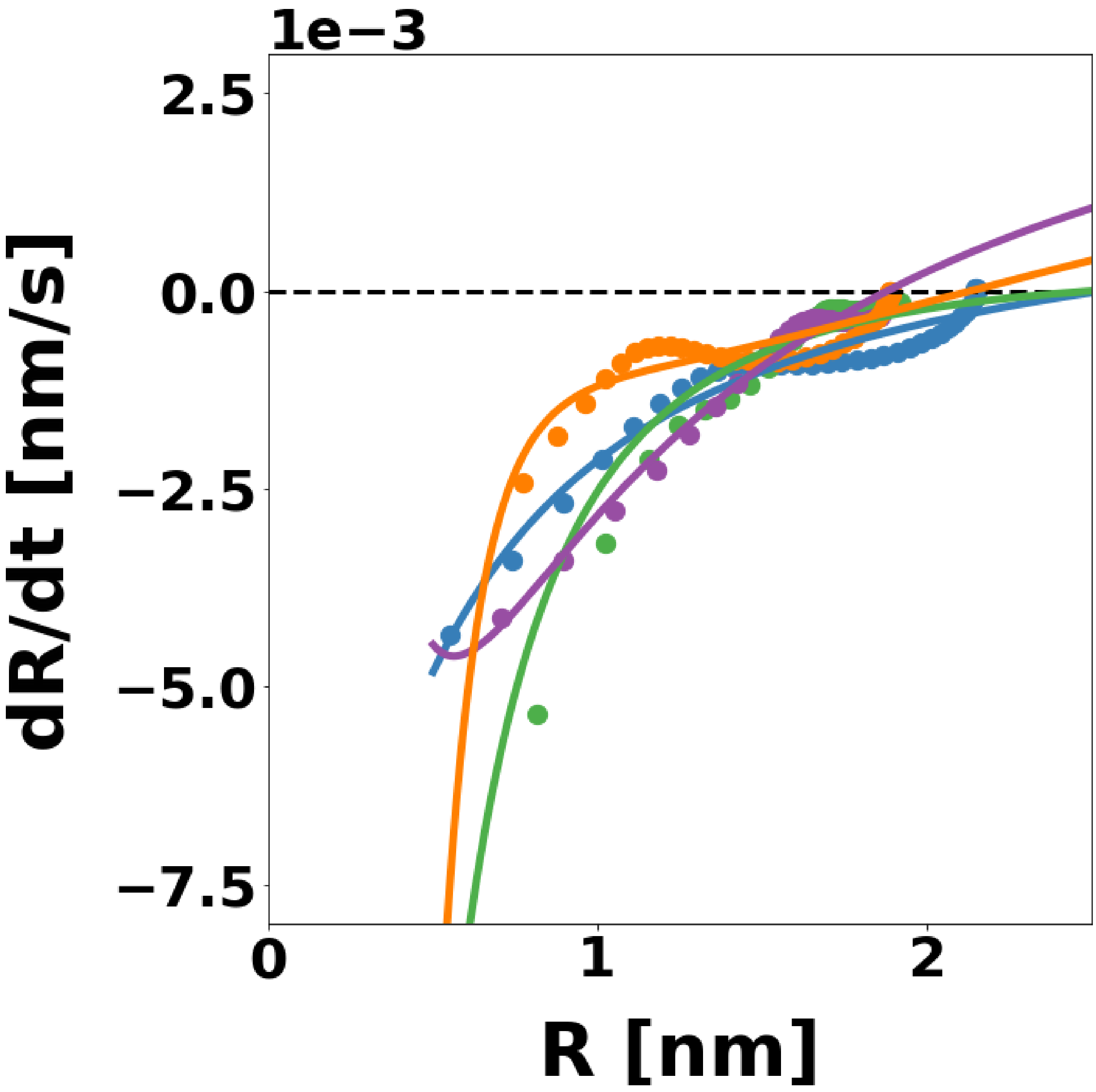

Supplemental Figure 2. Demonstration of model fits to a randomly selected set of particles. Correspondingly colored points and lines represent the experimental data and fit for an individual particle, respectively. Note the up-turn predicted by the fit at small radius in the purple particle – this is not physical and is likely a result of not having enough measurements at small R to properly represent the data.

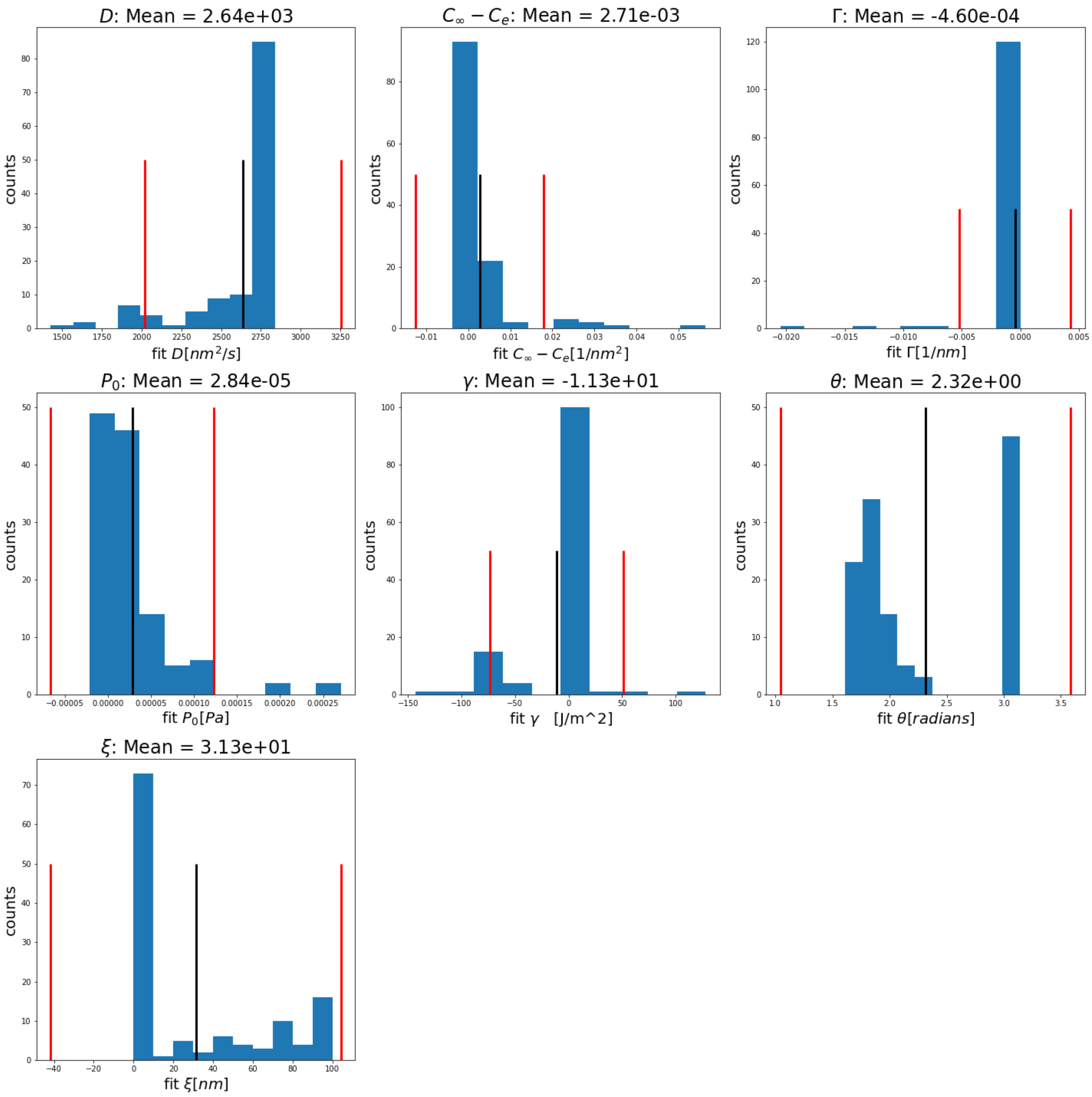

Supplemental Figure 3. Histogram of raw parameter values taken from fitting 125 particles to Equation 3.

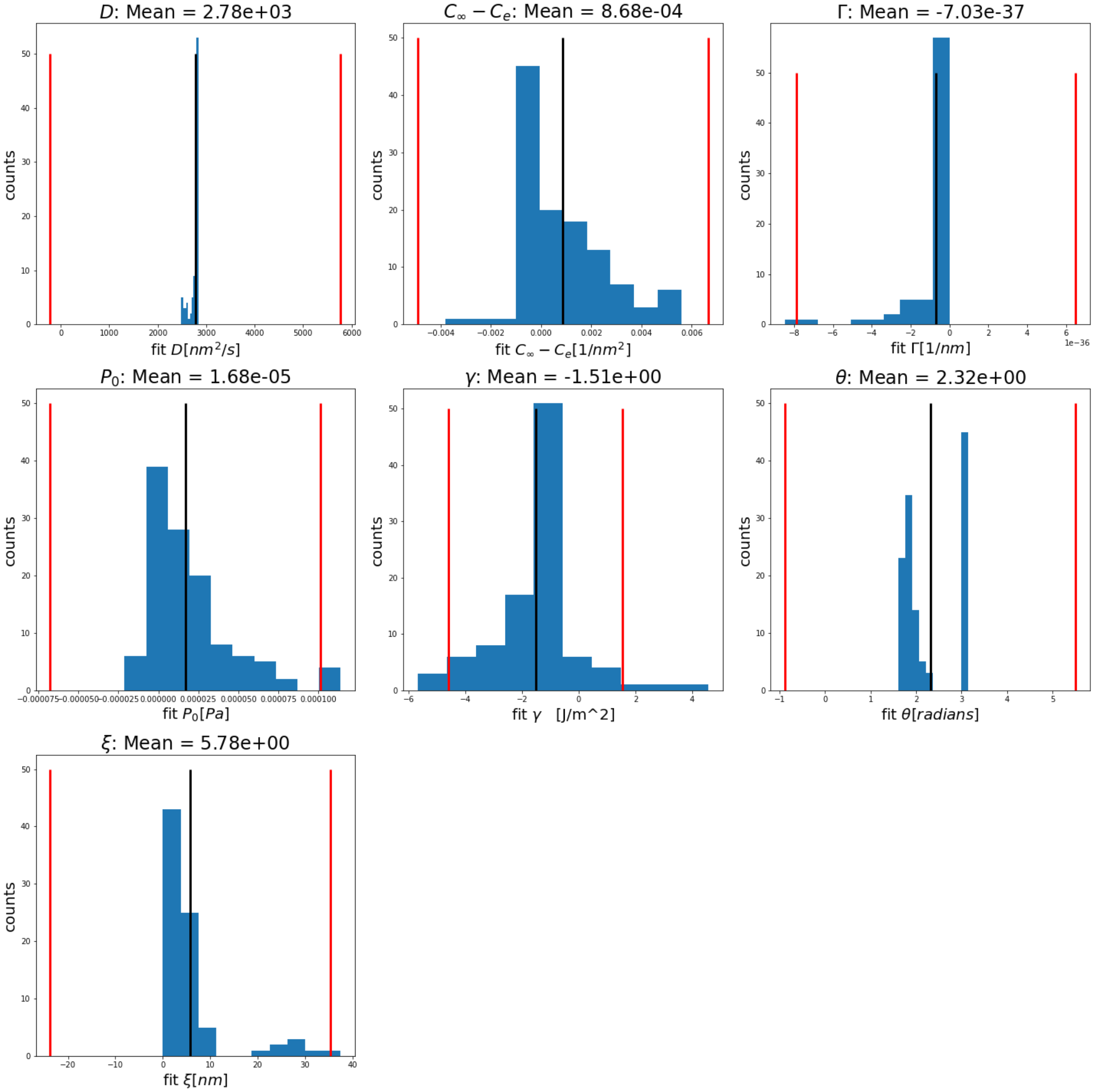

Supplemental Figure 4. Histograms of parameter values after removing outliers. Outliers were defined by calculating the median absolute deviation of each value, and then using a modified *z*-score of 3.5 as a threshold.

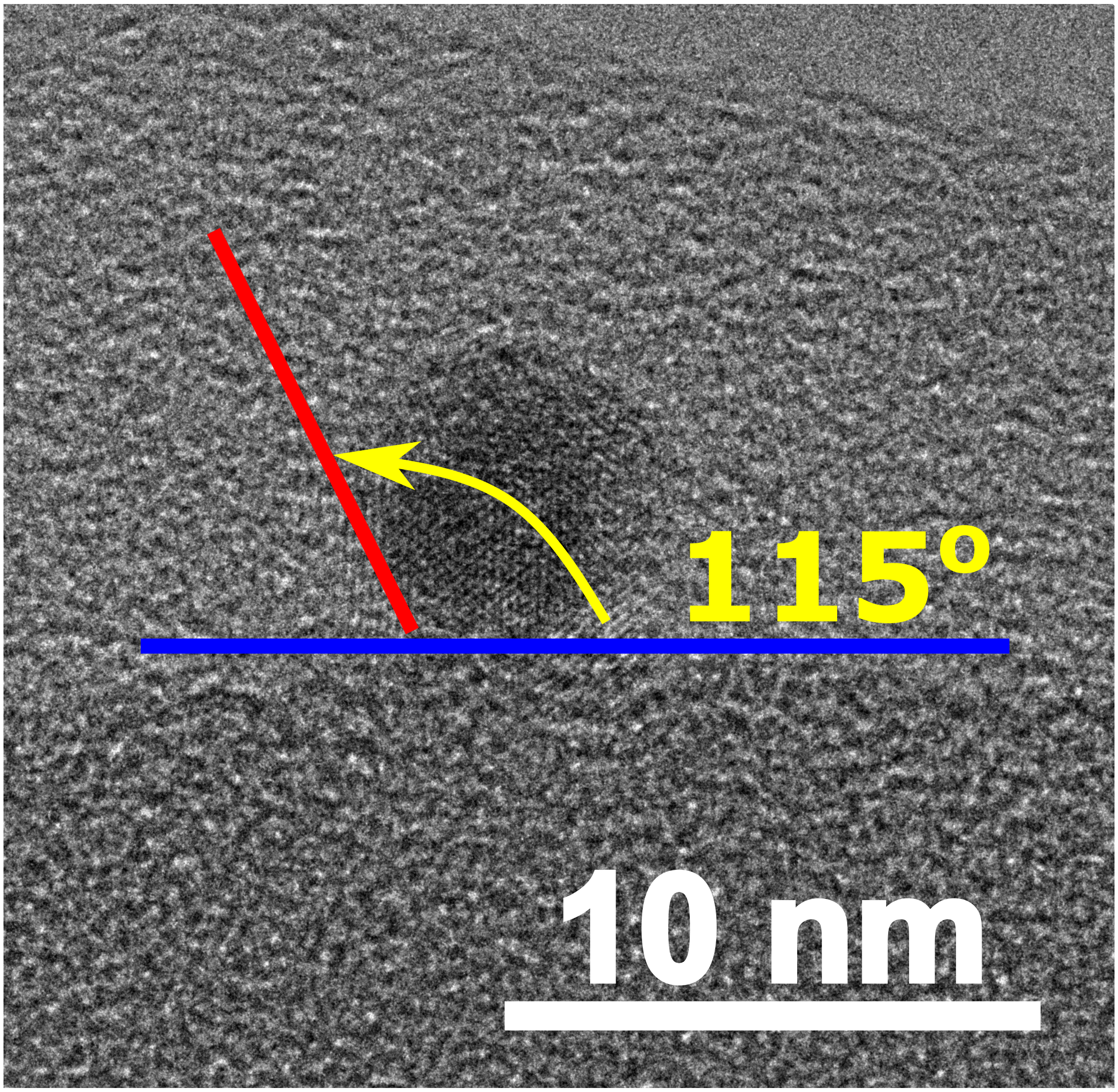

Supplemental Figure 5. Image showing the measurement of contact angle form an experimental TEM image. Gold particles were drop cast onto SiO_2 Stöber Spheres, plasma cleaned via the method described in the text, and imaged. The contact angle could be directly observed for particles deposited perpendicular to the imaging direction.

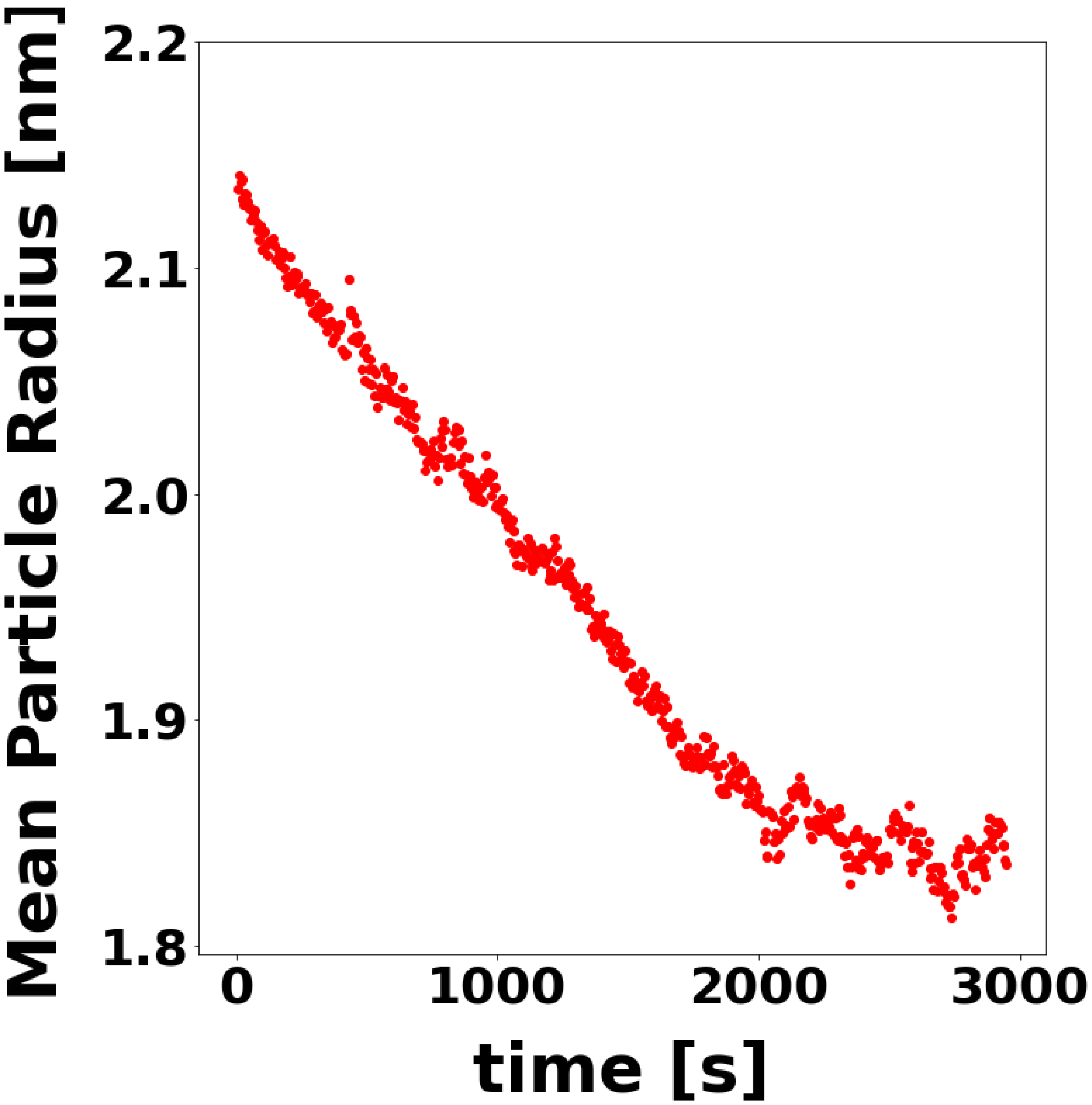

Supplemental Figure 6. Mean particle size a function of time. The plot shows that the decrease in particle size slows down as time progresses, signifying that a stable particle size is reached after a transient period of evaporation.

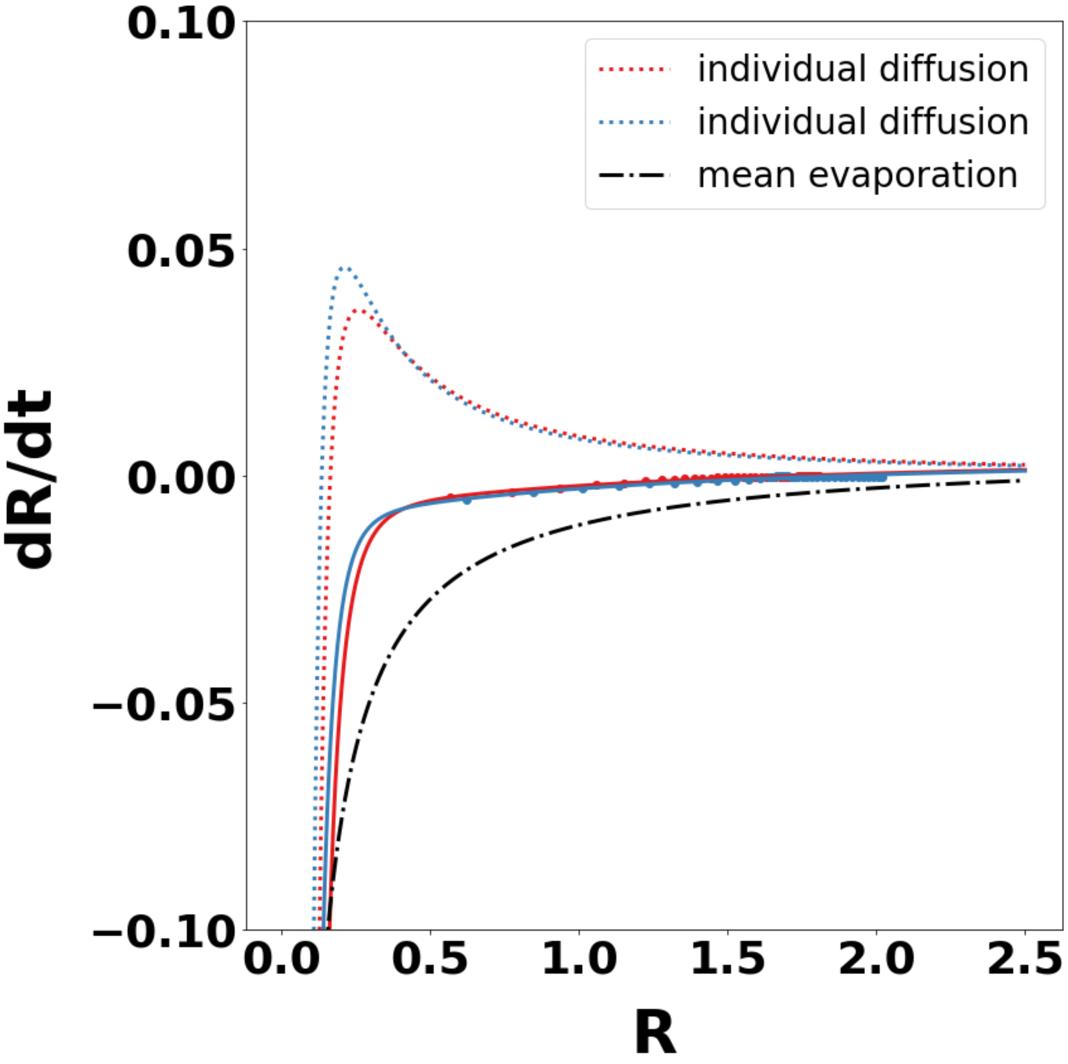

Supplemental Figure 7. Individual fits to the diffusion component of the red and blue particles in Figure 3. The diffusion curve reaches a maximum near 0.5nm. Particles larger than this grow due to the relatively large concentration of adatoms on the support. In contrast, small particles rapidly shrink as the Gibbs-Thomson effect drives their interfacial concentration to become larger than the adatom concentration.

	$C_\infty - C_e \left[\frac{1}{nm^2}\right]$	$\Gamma \left[\frac{1}{nm}\right]$
	7.6 e -4	3.6 e -9
	9.5 e -4	1.16 e -4
	8.5 e -4	8.5 e -5
All that shrink	8.7 e -4	1 e -4
Don’t shrink	7 e -4	1e-6

Supplemental Table 2. Fit values for particles shown in Figure 3 of the main text. Colors correspond to the colored particles in the figure. A capillary length (Γ) for the green particle cannot be accurately calculated since it does not shrink significantly